Transition to time-dependent flow in highly viscous horizontal convection

Lennart Ramme* and Ulrich Hansen
Institut für Geophysik, WWU Münster, Corrensstraße 24, 48149 Münster, Germany

(Received 17 March 2019; published 10 September 2019)

Horizontal convection is studied numerically in two dimensions for the case of an infinite Prandtl number and shear-free boundary conditions on all sides. Three different temperature distributions are applied at the top boundary. Steady states become unstable, giving way to unsteady flow with increasing Rayleigh number Ra. The transition to time-varying flow depends on the heating configuration. For $\mathrm{Ra} \geqslant 5 \times 10^9$ simulations show a time-dependent flow behavior for a linearly varying temperature at the top, whereas other temperature distributions show this transition at even lower Rayleigh numbers. The scaling laws of heat flow and circulation strength are investigated and the results indicate that both are changed by the upcoming time-dependent flow. While in the steady boundary layer flow regime the heat flux scales as $\mathrm{Ra}^{1/5}$, the exponent increases to a value of approximately 0.25 in the unsteady regime. A similar transition is observed for the circulation strength. The observed scaling laws are in good agreement with established theories in both the steady and unsteady regimes. After the transition, the flow shows a periodic oscillation of the boundary layer circulation, which turns into a more irregular flow behavior as the Rayleigh number is increased further. We conclude that, even for an infinite Prandtl number, horizontal convection exhibits unsteady flow at sufficiently high Rayleigh numbers and that this flow resembles the turbulent circulation at low Prandtl numbers.

DOI: 10.1103/PhysRevFluids.4.093501

I. INTRODUCTION

Besides the famous Rayleigh-Bénard and vertical convection, there is the concept of horizontal convection [1], which has been of growing interest in recent studies (e.g., in Ref. [2,3]). In this type of convection a temperature variation is applied at one horizontal boundary, while all other boundaries are kept insulating. This results in a characteristic asymmetric flow structure [4]. The fluid flows along this boundary from the warm to the cold region, if the temperature is prescribed from above and analogously from the cold to the warm region, if a temperature configuration is applied from below. Rossby was one of the first who studied this type of flow in both experiments and numerical simulations [5,6] and he derived that heat flow and circulation strength scale as $\mathrm{Ra}^{1/5}$ in a wide range of Rayleigh (Ra) and Prandtl numbers (Pr). This proved the conclusion of Jeffreys [7] wrong, namely, that convection can only be maintained when the heating is applied from below the cooling. Since then, various studies have been performed to expand the Rayleigh and Prandtl number ranges and to give theoretical explanations for the observed features [8–12]. Hughes and Griffiths [2] provide a comprehensive review of the different observed flow structures and scaling regimes in horizontal convection.

A key feature of horizontal convection is that, for fixed Prandtl number and increasing Rayleigh numbers, there are transitions between different regimes. For small Rayleigh numbers the system is

*lennart.ramme@uni-muenster.de

dominated by diffusion, the circulation cell is nearly symmetric, and the return flow occurs at the opposite boundary. As the Rayleigh number increases, the circulation becomes stronger and most of the flow is confined to a thin layer near the boundary at which the temperature forcing is applied. Chiu-Webster *et al.* [13] state that this steady intrusion will dominate horizontal convection for large Prandtl numbers. At small Prandtl numbers there is a critical Rayleigh number above which the flow becomes unsteady in the region of the descending (or rising, if the forcing boundary is the bottom one) plume. In general, several studies indicate that this transition appears for sufficiently small Prandtl numbers and a fixed Rayleigh number or at a fixed Prandtl number with sufficiently high Rayleigh numbers [2,14]. A number of studies show that, with a finite Prandtl number and above a critical Rayleigh number, horizontal convection flows will involve unsteady areas with very efficient mixing [15–18]. More recent work was done regarding the stability of horizontal convection restricted to Prandtl numbers between 1 and 10 [3,19,20], which consistently found a transition to unsteady behavior. Tsai *et al.* [19] describe an initially periodic flow which turns chaotic as the Rayleigh number is further increased. So far, a transition to unsteady flow at infinite Prandtl number has not been observed.

More comprehensive theories have been developed to explain not only the steady boundary layer regimes, which can be described by the Rossby scalings, but also the unsteady and turbulent regimes found at different Rayleigh and Prandtl number ranges. Hughes *et al.* [10] provide a recycling box model for high Rayleigh numbers, where the circulation strength scales as $\mathrm{Ra}^{3/10}$. More recently, Shishkina *et al.* [11] applied the Grossmann-Lohse [21] ansatz to horizontal convection and presented scaling laws for a number of different flow regimes. With this approach they match the Rossby scalings [5] of the steady boundary layer regime as well as the upper bound for the heat flux scaling of $\mathrm{Ra}^{1/3}$ for very large Rayleigh numbers (greater than 4×10^{15}) proposed by Siggers *et al.* [22]. Furthermore, it was stated that for large Prandtl numbers ($\mathrm{Pr} > 10$) the heat flux would scale as $\mathrm{Ra}^{1/4}$, confirming the results of Sheard and King [23] and Shishkina and Wagner [12].

Most studies on horizontal convection target systems like oceans or planetary atmospheres, which are cooled at the poles and heated at the equator [24,25]. In contrast to these fast moving systems, the case of an infinite Prandtl number was considered in only a few studies [13]. Horizontal convection in highly viscous media plays a role in the glass industry, where heating and the influx of new, cooler material are at the same horizontal level [26] and also geodynamical applications with a horizontal temperature difference are conceivable. At the core-mantle boundary horizontal temperature differences are created through cold subducting slabs on the one hand and regions of upwelling hot material on the other hand [27]. Therefore, a deeper investigation of horizontal convection at infinite Prandtl number is of high interest. Chiu-Webster *et al.* [13] tested the robustness of the Rossby scalings for this case in the Rayleigh number range from 10^6 up to 10^{10}. They provide results for rigid and shear-free conditions along that boundary where the temperature forcing is applied, while all other boundaries are rigid in both cases. These simulations remain steady over the entire Rayleigh-number range and show that the scaling laws are valid for steady flows in the highly viscous case as well. In additional simulations Chiu Webster *et al.* [13] use a finite but high Prandtl number ($\mathrm{Pr} = 10^5$) and rigid boundary conditions on all sides. Here the flow becomes unsteady for high Rayleigh numbers ($\mathrm{Ra} \geqslant 3 \times 10^8$). The fact that horizontal convection can exhibit unsteady flow at such high Prandtl numbers indicates that an infinite Prandtl number could also lead to time-dependent flow at sufficiently high Rayleigh numbers.

In this paper we investigate the case of an infinite Prandtl number using direct numerical simulations (DNS), where we test the influence of different heating distributions along the upper horizontal boundary. This has been the topic of only a few studies [6,28] and it is assumed that different temperature distributions will mainly lead to the same results, as long as they are smooth and monotonic [13]. Indeed, similar flow regimes are approached with the different configurations tested here, but the strength of the overturning circulation and the surface heat flow strongly vary. Furthermore, we show that there is a transition to unsteady flow behavior also in the highly viscous case of horizontal convection and this transition depends on the temperature configuration as well. In the following section we present the underlying equations in Sec. II A and the numerical solution

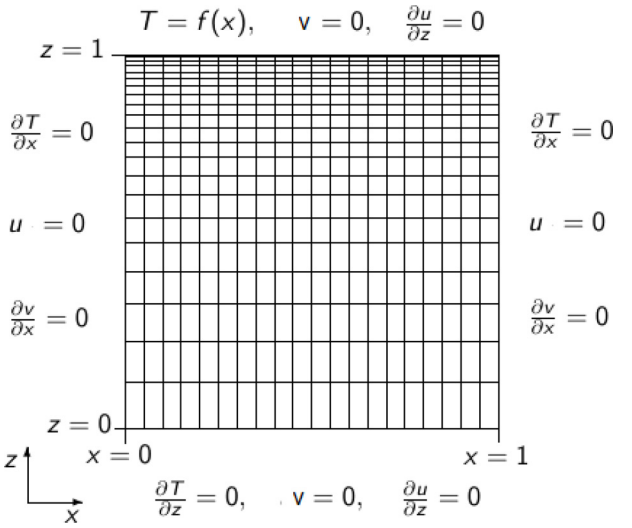

FIG. 1. Model setup for the numerical simulations showing the different boundary conditions and a simplified grid including 21 elements in each direction and an exponentially decreasing grid spacing from $z = 0$ to $z = 1$. Actual grids have at least 101×101 and up to 251×251 elements.

scheme and model setup in Sec. II B. The presentation of results is divided into a general description of the flow (Sec. III A), followed by a closer look at the scaling laws (Sec. III B) and the unsteady circulation (Sec. III C). Section IV discusses and summarizes the findings.

II. MODEL

We consider a two-dimensional model with shear-free boundary conditions on all sides. Boundaries that are not set to a certain temperature are insulating. Various heating configurations are applied to the top wall and all of them have the same total temperature difference between the coldest and the warmest part. The aspect ratio of the model box will be $A = 1$ for all runs. The boundary conditions and a schematic sketch of the grid are displayed in Fig. 1.

A. Mathematical description

The underlying equations in the Boussinesq approximation, where density variations contribute only to the buoyancy term while all other parameters are kept constant, can be written as

$$\frac{1}{\mathrm{Pr}}\left(\frac{\partial \boldsymbol{u}}{\partial t} + (\boldsymbol{u}\cdot\boldsymbol{\nabla})\boldsymbol{u}\right) = -\boldsymbol{\nabla}p + \nabla^2\boldsymbol{u} + \mathrm{Ra}T\hat{\boldsymbol{e}}_z, \tag{1}$$

$$\boldsymbol{\nabla}\cdot\boldsymbol{u} = 0, \tag{2}$$

$$\frac{\partial T}{\partial t} + (\boldsymbol{u}\cdot\boldsymbol{\nabla})T = \nabla^2 T. \tag{3}$$

Here $\boldsymbol{u} = (u, v)$ denotes the two-dimensional velocity field, t is the time, p is the pressure, and T is the temperature. For the nondimensionalization of these equations, lengths are divided by the box length L and time is divided by the thermal diffusion time L^2/κ over that length, where κ is the thermal diffusivity. Furthermore, velocity, temperature, and pressure are nondimensionalized by κ/L, ΔT, and $\rho_0\nu\kappa/L^2$, respectively, with ρ_0 the density at $T = 0$ and ν the kinematic viscosity. The Prandtl number $\mathrm{Pr} = \nu/\kappa$, which describes the ratio between kinematic viscosity and thermal diffusivity, is considered to be infinite, leading to a very viscous fluid. The Rayleigh number is

defined through

$$\mathrm{Ra} = \frac{\alpha g \Delta T L^3}{\nu \kappa}, \tag{4}$$

where α is the thermal expansion coefficient and g the gravitational acceleration. In a two-dimensional system, the introduction of a scalar stream function ψ, with $u = \partial\psi/\partial z$ and $v = -\partial\psi/\partial x$, reduces Eqs. (1)–(3) to

$$\nabla^4 \psi = \mathrm{Ra} \frac{\partial T}{\partial x}, \tag{5}$$

$$\frac{\partial T}{\partial t} = \frac{\partial \psi}{\partial x}\frac{\partial T}{\partial z} - \frac{\partial \psi}{\partial z}\frac{\partial T}{\partial x} + \nabla^2 T, \tag{6}$$

while automatically satisfying that the fluid is incompressible.

In order to classify the flow we stick to the definitions of Ref. [13] and characterize the circulation strength through the Péclet number defined as

$$\mathrm{Pe} \equiv \psi_{\max}. \tag{7}$$

The maximum of the stream function will in most runs be located in the top left corner, where the fluid turns around and either descends in a plume or flows into the opposite direction in a shallow intrusion. The global heat transfer is defined through the unsigned Nusselt number

$$\mathrm{Nu} \equiv \int_0^1 \left| \frac{\partial T}{\partial z}\bigg|_{z=0} \right| dx, \tag{8}$$

which includes the absolute value of the heat transfer at every point of the upper boundary. This is necessary because in runs where the flow evolves to a steady state the net heat flow through the upper boundary is zero, since all other boundaries are insulating. Depending on the Rayleigh number, different numbers of elements are used, which influences the calculation of the Nusselt number. A Richardson extrapolation is applied to account for this and to achieve independence of the grid. Following the literature [5,11,13], the Péclet and Nusselt numbers should scales as

$$\mathrm{Pe}, \mathrm{Nu} \sim \mathrm{Ra}^{1/5} \tag{9}$$

for steady flow, but the scaling laws might deviate as the convection becomes unsteady. The Rossby scalings (9) result from the assumption that the vertical scale of the velocity at the upper boundary equals the thickness of the thermal boundary layer at the top.

B. Numerical method

A finite-element method is applied to solve the equations numerically. For spatial discretization a nonconforming rectangular element is used for Eq. (5), while a bilinear rectangular element with upwinding correction is applied to discretize Eq. (6) (see Ref. [29] for more information on the spatial discretization). The temporal discretization is described in Ref. [30]. It uses a predictor-corrector method with a fully implicit predictor step and a Crank-Nicolson corrector step. The numerical scheme has been validated in a benchmark comparison in terms of mantle convection [31].

For $\mathrm{Ra} < 10^8$, 101×101 elements are used, with a fine grid near the upper boundary and an exponentially increasing grid spacing towards the bottom of the system (very small Rayleigh numbers are calculated with an equidistant grid because of the symmetric flow structure). Consequently, the strong gradients in the boundary layer are sufficiently resolved. For $\mathrm{Ra} \geqslant 10^8$ the number of elements is increased to 161×161 and at $\mathrm{Ra} \geqslant 5 \times 10^9$ a number of 251×251 elements are used to ensure a good resolution in the very thin boundary layer. For the high Rayleigh numbers that create irregular downwellings on the left side it may be appropriate to also use a refined grid in the

region of the descending plume. However, test runs show that the effect on the general flow behavior is small and the scaling parameters are not affected.

III. RESULTS

Three different temperature distributions were applied at the top boundary: the linear profile

$$T = x,$$

the corner profile

$$T = \begin{cases} 0, & 0 \leqslant x < 0.2 \\ \text{insulating}, & 0.2 \leqslant x \leqslant 0.8 \\ 1, & 0.8 < x \leqslant 1, \end{cases}$$

and the step profile

$$T = \begin{cases} 0, & 0 \leqslant x < 0.5 \\ 1, & 0.5 \leqslant x \leqslant 1. \end{cases}$$

With these configurations we performed numerical experiments for Rayleigh numbers between 10^4 and 10^{10}. The calculations were terminated when a final steady state was reached and no further significant changes in the heat transfer and circulation strength occurred. In cases where the flow remained unsteady and both parameters strongly varied for every time step, we calculated means over a large number of time steps instead.

We will begin in Sec. III A by describing the overall flow behavior and the temporal evolution of the runs. In Sec. III B the scaling laws for the circulation strength and the heat flow are shown. In Sec. III C the time-dependent flow is investigated in detail.

A. Flow structure in highly viscous horizontal convection

Hughes and Griffiths [2] summarize the results of numerous studies and divide horizontal convection flows into three different regimes. The diffusion regime for small Ra, the intrusion regime for large Pr and intermediate to high Ra, and the unsteady entrainment regime for high Ra and Pr $<$ 10–100 (the critical value increases with increasing Ra). For an infinite Prandtl number, Chiu-Webster *et al.* [13] were able to observe the diffusion and the intrusion regime for Ra $\leqslant 10^{10}$ but not the entrainment regime.

In general, all of our heating configurations result in similar flow structures. The step profile, however, results in a significantly stronger circulation. Figure 2 shows the final states of convection for Ra $= 10^4$, 10^8, and 10^{10} as obtained with the linear and the step profile. For small Ra, like in Figs. 2(a) and 2(d), the typical features of the diffusion regime, i.e., a weak, almost symmetric circulation extending throughout the whole box, can be observed. At around Ra $= 10^6$ a return flow begins to form as an intrusion beneath the surface flow. The transition into this regime is smooth and cannot be assigned to a particular value of the Rayleigh number. Nevertheless, it appears in the same range of Ra for all three temperature distributions. As the Rayleigh number increases further, the circulation cell thins and is shifted towards the upper boundary. This resembles a flow structure as shown in Fig. 2(b), which is a typical example for the intrusion regime. For all three heating configurations there is a certain Rayleigh number above which the flow becomes time dependent, but the specific values vary depending on the forcing at the top boundary. The step profile exhibits unsteady flow behavior at the lowest value of Ra $= 9 \times 10^7$, whereas the linear profile still leads to a steady flow until it first shows time dependence at Ra $= 5 \times 10^9$. The corner profile first shows time-dependent flow at an intermediate value of Ra $= 7 \times 10^8$. The unsteady behavior at relatively low Ra is characterized by an oscillation of the boundary layer flow as shown in Fig. 2(e), whereas the runs with the highest Ra show irregular downwellings reaching the bottom of the model

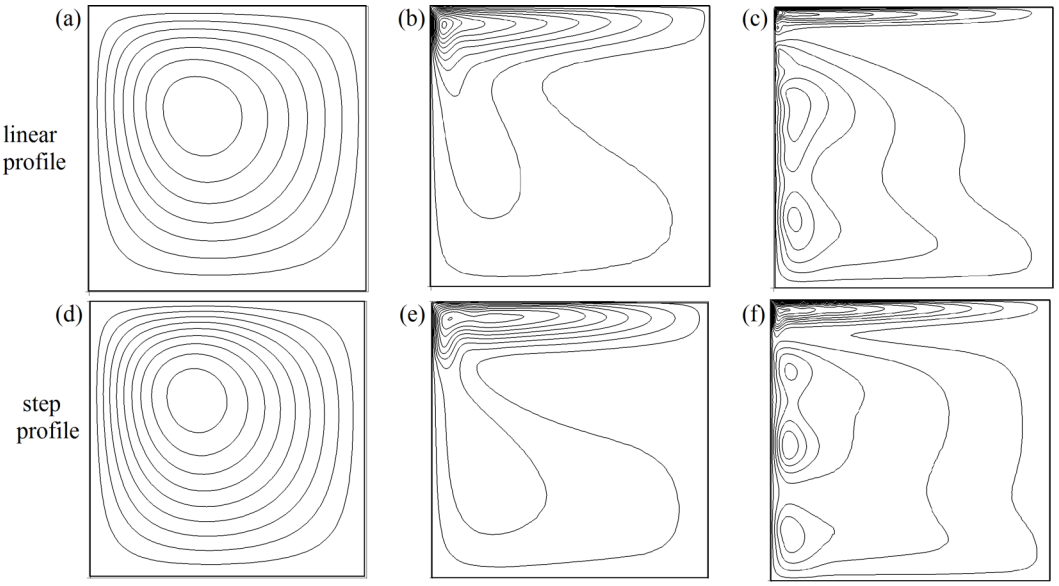

FIG. 2. Streamlines of the linear and the step profile for (a) and (d) $\mathrm{Ra} = 10^4$, (b) and (e) $\mathrm{Ra} = 10^8$, and (c) and (f) $\mathrm{Ra} = 10^{10}$ after a thermal equilibrium is reached. Graphics (a), (b), and (d) evolved to a steady state, while (c), (e), and (f) remained unsteady, so these figures represent only snapshots of a temporal behavior. The intervals between streamlines are (a) and (d) 0.5, (b) and (e) 5, (c) 15, and (f) 25.

[Figs. 2(c) and 2(f)]. We therefore divide horizontal convection flows into four different regimes which can all be seen in Fig. 2: the diffusion regime in Figs. 2(a) and 2(d), the intrusion regime in Fig. 2(b), the unsteady time-periodic regime in Fig. 2(e), and a chaotic regime in Figs. 2(c) and 2(f). Figures 2(c), 2(e), and 2(f) are chosen to be representative snapshots of an unsteady circulation. A detailed description of the time-dependent flow will be given in Sec. III C.

The route towards the final state strongly depends on the initial temperature of the model. If it is below the thermal equilibrium temperature that is ultimately reached, a strong boundary layer flow develops with almost no convection in the lower part. Consequently, the interior of the system is heated through diffusion only and a long time is needed to reach the final state. If, on the other hand, the initial temperature is higher, a strong downwelling forms which cools the interior efficiently through convection and weakens as the final state is reached. The final steady states are in general identical, but less time is needed to reach it with a higher initial temperature. For all results presented in this study (unless stated otherwise) the initial temperature is set to a value slightly above the expected final temperature of the interior, thus minimizing the time needed to reach the final states. In Fig. 3 the temporal evolution of Nu and Pe for selected Rayleigh numbers and the step profile is depicted: The typical shape of the curves, high initial values followed by a subsequent decrease, is a consequence of the warm initial temperature. A colder start would result in lower parameter values followed by a slow increase. When a steady state is reached, both parameters approach a constant value which increases with Ra. The onset of time dependence is reflected by fluctuations in Nu and Pe within a certain range which allows one to calculate a mean. The Péclet number varies much more than the Nusselt number because it is determined through a single value of the stream function, whereas the Nusselt number is calculated by averaging over a large number of points.

B. Scaling laws

The Ra dependences of $\mathrm{Nu}\,\mathrm{Ra}^{-1/5}$ and $\mathrm{Pe}\,\mathrm{Ra}^{-1/4}$ are shown in Fig. 4 to investigate the scaling laws of heat flux and circulation strength. In the steady runs the Rossby scaling $\mathrm{Nu} \sim \mathrm{Ra}^{1/5}$

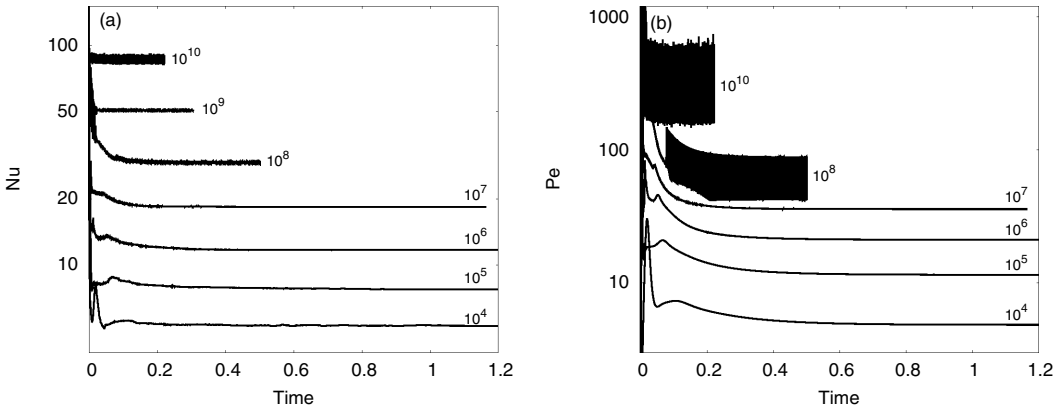

FIG. 3. Temporal evolution of (a) Nu and (b) Pe in the step profile. Labels in the plots indicate Ra. In (b) $\mathrm{Ra} = 10^9$ is not shown because it overlaps with the adjacent values.

[horizontal dashed line in Figs. 4(a), 4(c), and 4(e)] is approached asymptotically with increasing Rayleigh number, similar to what was observed by Chiu-Webster *et al.* [13]. As the flow becomes unsteady for higher Rayleigh numbers, the scaling deviates and tends towards a higher exponent. This can be seen most clearly using the step profile [Fig. 4(e)], where the dotted line, describing a scaling of $\mathrm{Nu} \sim \mathrm{Ra}^{1/4}$, fits the data better in the high-Ra range. The two runs with the highest

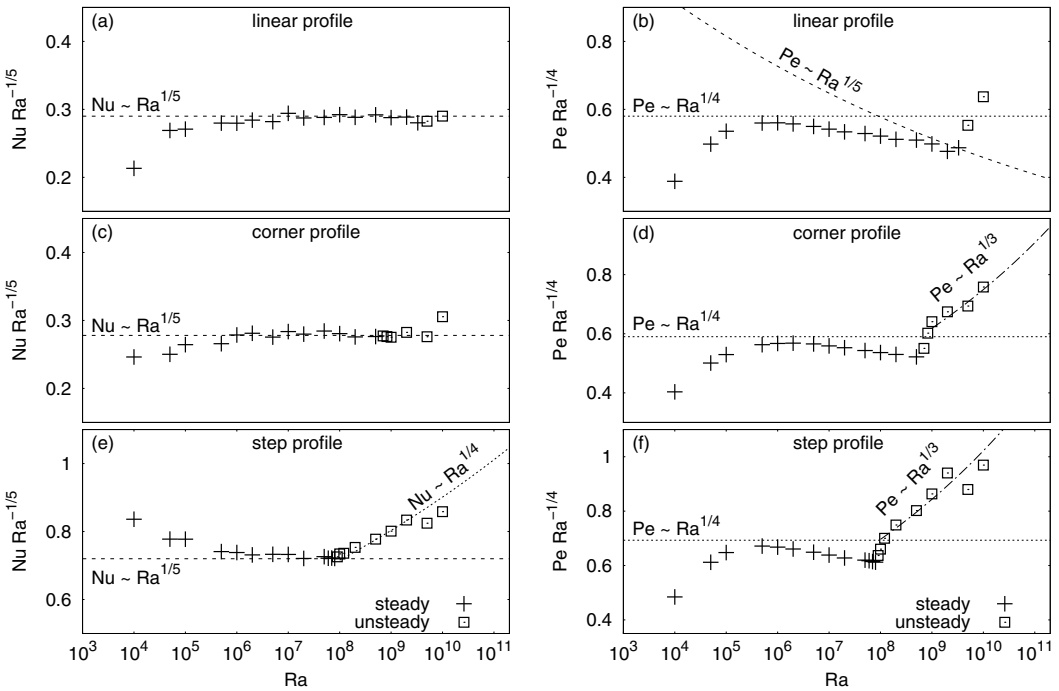

FIG. 4. Scaling laws of (a), (c), and (e) heat flux and (b), (d), and (f) circulation strength for the three heating configurations applied at the top boundary. Crosses indicate runs reaching a steady state and squares stand for runs that remain unsteady. The lines represent different scaling laws, indicated by the labels in the plot.

Rayleigh numbers (5×10^9 and 10^{10}) appear to have a heat flux and circulation strength that are slightly too small when the step profile is used [Figs. 4(e) and 4(f)]. The reason for this is unclear, but possible explanations are the higher grid resolution used at these Ra, the transition from a periodic to a chaotic time dependence (see Sec. III C), and the influence of the strong jump in temperature at $x = 0.5$ in this configuration. The values of the two points do not influence the overall picture of a clear change in the scaling behavior after the transition from steady to unsteady flow.

In contrast to the Nusselt number, the Péclet number does not approach the Rossby scaling of $\mathrm{Pe} \sim \mathrm{Ra}^{1/5}$ in the steady regime [dashed line in Fig. 4(b)]. The horizontal dotted lines have a proportionality of $\mathrm{Pe} \sim \mathrm{Ra}^{1/4}$, but the actual values in the steady boundary layer regime (steady runs with $\mathrm{Ra} \geqslant 10^6$) follow a path between both scaling laws. Similar to what was observed for the Nusselt number, the scaling of the circulation strength also changes as the unsteady flow emerges. The Péclet number grows faster and the exponent in the scaling law increases. In Figs. 4(d) and 4(f) the dash-dotted line has a slope of $1/3$, but with such few data points slightly higher or lower exponents fit equally well. A similar transition is visible for the linear profile in Fig. 4(b) for the two runs with the highest Ra. Investigation of the flow at $\mathrm{Ra} > 10^{10}$, which would help to determine a more precise value of the exponent, was not possible within the frame of this study.

C. Characteristics of the time-dependent flow

When the circulation becomes unsteady instabilities are generated in the cooled region which travel towards the left sidewall and then descend into the interior. At the lowest Rayleigh numbers that show this behavior (around $\mathrm{Ra} = 10^8$ for the step profile) the general flow structure looks similar to the flow in the steady intrusion regime which occurs at the same Rayleigh number for the linear profile [compare Figs. 2(b) and 2(e)]. The major difference are instabilities within the boundary layer. These instabilities are formed periodically and they slightly deform the streamlines in their vicinity, leading to an oscillation of the circulation strength. The descending plumes penetrate only down to shallow depths and the major return flow still takes place as an intrusion right below the surface flow. The periodic behavior of the instabilities can be made visible through the phase plot in Fig. 5(a), showing the oscillation of the Péclet number. As the Rayleigh number is increased, the generation of instabilities may become more complex. For example, in Fig. 5(b) for $\mathrm{Ra} = 2 \times 10^8$ a doubling of the period can be observed. However, all other phase plots referring to the periodic regime exhibit simple oscillations as in Fig. 5(a). At very high Ra instabilities are randomly generated and no periodicity can be detected. This leads to a more or less chaotic distribution of points in the phase space, as can be seen in Fig. 5(c). In these cases the downwellings penetrate the whole depth of the model as in Fig. 2(c) and strongly enhance the mixing ability of the convection, yet a major part of the return flow is still confined to a strong boundary layer flow. Figure 5(d) shows the phase plot for $\mathrm{Ra} = 10^{10}$ using the linear profile. Here certain trajectories are visited more frequently and all curves have a similar shape. Cases like this may mark the transition into the chaotic regime, since runs with lower values of Ra can be assigned to the periodic regime, while higher values of Ra lead to the more chaotic phase plots as in Fig. 5(c).

In contrast to the steady runs, where the same final state is reached independently of the initial temperature, we observed one case of unsteady flow with sensitivity to the initial conditions. For $\mathrm{Ra} = 2 \times 10^9$, applying the step profile, the evolution of the time-dependent flow depends on the initial temperature of the model. In Figs. 6(a)–6(d) the time history of the Nusselt number is depicted for different starting conditions. For a cold initial temperature below a critical value, being between $T = 0.07$ and $T = 0.076$, the resulting Nusselt number is approximately 10% smaller than compared with the case of a higher initial temperature. Furthermore, runs with a cold initial temperature [Figs. 6(a) and 6(b)] result in flows with a strong and more irregular variation of the output parameters that can be characterized through a phase plot similar to Fig. 5(c). Differently, flows with higher initial temperatures [Figs. 6(c) and 6(d)] end up in a more periodic circulation with weaker variations comparable to Fig. 5(a). The existence of two different convection regimes becomes even clearer when the temperature of the final states is compared. In Fig. 6(e) the

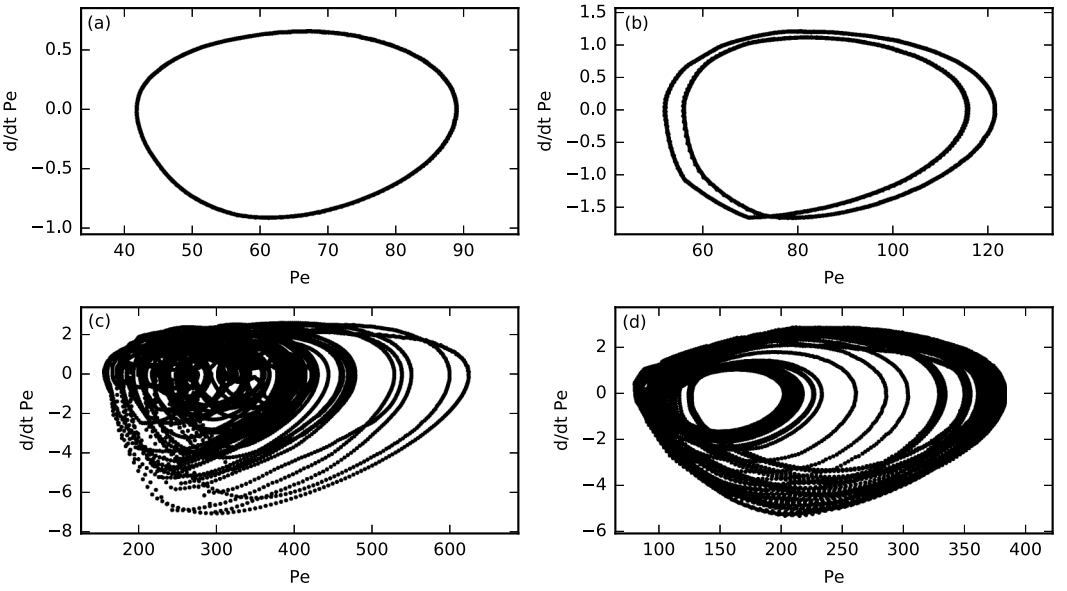

FIG. 5. Phase plots of the Péclet number for (a) $\mathrm{Ra} = 10^8$, (b) $\mathrm{Ra} = 2 \times 10^8$, and (c) $\mathrm{Ra} = 10^{10}$ with the step profile. In (d) the linear profile is used for the same Rayleigh number as in (c): $\mathrm{Ra} = 10^{10}$. Time derivatives are calculated with a centered-difference approximation using the number of the time step instead of the time in the denominator. This neglects the variable step size, but accounts for the loss of significance due to the very small time steps. The qualitative appearance of the phase diagrams is not affected.

depth dependence of the temperature at $x = 0.5$ is presented. The two runs with a colder initial temperature result in a final temperature of $T = 0.06$, while the two warmer runs lead to $T = 0.08$ for $0 < z < 0.8$. This is a particular feature of the case $\mathrm{Ra} = 2 \times 10^9$ employing this specific forcing. Smaller Ra always result in a periodic oscillation, whereas higher Ra lead to irregular fluctuating downwellings. For the other temperature configurations a dependence on the initial condition was not observed.

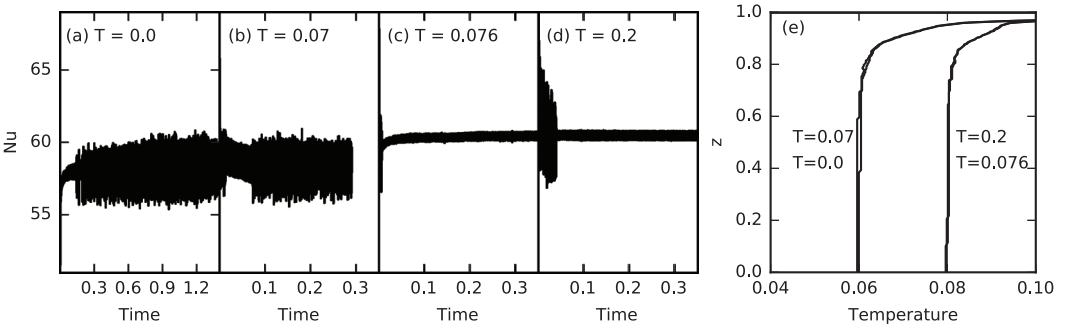

FIG. 6. (a)–(d) Temporal evolution of the Nusselt number for $\mathrm{Ra} = 2 \times 10^9$ and different initial temperatures in the step profile. (e) Depth dependence of the temperature in the final states of convection at $x = 0.5$. The labels in the plot (e.g., $T = 0.0$) mark the initial temperature of the run. The lines for $T = 0.2$ and $T = 0.076$ lie exactly on top of each other. The ones of $T = 0.0$ and $T = 0.07$ are also very similar to each other.

IV. DISCUSSION AND CONCLUSION

Horizontal convection at an infinite Prandtl number is studied numerically to better understand the influence of different types of temperature configurations applied at the top boundary. The general flow structure is investigated and special attention is given to the scaling laws of the heat flux and circulation strength.

The first important finding is that variations in the forcing have no significant impact on the resulting flow structure. Apparently, the flow structure of horizontal convection only weakly depends on the exact temperature configuration, as already suggested in [6,13]. In fact, even test runs with only 10% heating and the remaining 90% of the top boundary being cooled, as well as the opposite case of a large heated and a small cooled region, showed the typical asymmetric circulation of horizontal convection. Differently from the flow structure, the strength of the circulation and the heat flow can vary strongly when the different temperature forcings are applied. For example, the Nusselt number of the step profile is more than two times higher than for the linear profile. Differences in the Péclet number are smaller but still significant. While in the steady regimes the different forcing types have no great influence on the dependences of Nu and Pe on Ra, they do determine the value of Ra at which the transition to time-dependent flow occurs. Besides the influence on the value of heat flow and circulation strength, this is the main difference that is achieved through changes in the temperature configuration.

The emergence of a time-dependent flow has not yet been observed in horizontal convection at an infinite Prandtl number, i.e., for convection at vanishing mechanical inertia, as relevant for highly viscous material. A previous study of highly viscous convection by Chiu-Webster *et al.* [13] provides steady solutions for Rayleigh numbers up to 10^{10} and an infinite Prandtl number while also reporting a time-dependent convection at a finite, but very high, Prandtl number and at the same time applying rigid boundary conditions on all sides. This indicates that very viscous horizontal convection can become unsteady at very high Rayleigh numbers and that the boundary conditions play a crucial role for the transition point. We here show that using the same temperature configuration, i.e., the linear profile, a time-dependent flow evolves for $\mathrm{Ra} \geqslant 5 \times 10^9$, when all sides have shear-free boundary conditions. In further simulations, not shown here, we adapted our model to the boundary conditions of [13], having only the upper boundary shear-free. This led to unsteady flow at even smaller Rayleigh numbers than observed with all sides being shear-free. All this indicates that rigid boundaries in general make it easier to generate unsteady flow in horizontal convection at high Prandtl numbers.

Additional tests, increasing the number of grid elements, reducing and increasing the time step, and starting at different initial temperatures always resulted in a time-dependent circulation. Considering this and the fact that all our temperature configurations show a time-dependent flow at high Ra, we conclude that a transition to unsteady flow not only is a typical feature for finite Prandtl number horizontal convection but also dominates convection at an infinite Prandtl number. According to our calculations, all solutions will ultimately become unsteady in horizontal convection with sufficiently high Rayleigh number.

Every heating configuration applied in this study showed the same scaling laws of heat flow and circulation strength in the respective flow regimes. When the Rayleigh number was high enough ($\mathrm{Ra} \geqslant 10^6$), but not too high, so that the flow remained laminar, we observed a $\mathrm{Nu} \sim \mathrm{Ra}^{1/5}$ relation, in accordance with the well known Rossby scalings that were confirmed by numerous studies [5,6,8,9,13]. On the other hand, our results for the scaling of the circulation strength in the steady regime show deviations from the $\mathrm{Pe} \sim \mathrm{Ra}^{1/5}$ Rossby scaling, tending towards a higher exponent. Chiu-Webster *et al.* [13] observed a similar behavior in a way that the Rossby scaling was approached only for very high Rayleigh numbers and that the curve had a higher slope before as well. In our runs this is not achieved, because the flow becomes unsteady at a certain Rayleigh number.

As soon as convection becomes unsteady the scaling laws of both the heat flux and the circulation strength change, in agreement with the results of Sheard and King [23] for simulations with a lower

Prandtl number, who also observed higher exponents in the time-dependent regime. Especially for the step profile, it becomes clear that the heat flux then follows a $\mathrm{Nu} \sim \mathrm{Ra}^{1/4}$ dependence. Such a scaling law is in good agreement with the predictions of the Grossmann-Lohse ansatz applied to horizontal convection [11]. Shishkina and Wagner [12] conducted DNS of horizontal convection over a range of Rayleigh and Prandtl numbers and were able to observe this scaling law for sufficiently high Pr. We confirm the $\mathrm{Nu} \sim \mathrm{Ra}^{1/4}$ scaling for horizontal convection at infinite Prandtl number and above a critical Rayleigh number, whose exact value depends on the heating configuration.

The change in the scaling law of the circulation strength is even more pronounced. As soon as the flow becomes unsteady, the circulation strength grows faster with increasing Rayleigh number and may be described by a $\mathrm{Pe} \sim \mathrm{Ra}^{1/3}$ scaling law. A similar relation is predicted by the theoretical model of Ref. [10], which was derived for a turbulent plume at the sidewall. All this implies that the Rossby scalings are only valid for the steady regime of horizontal convection at infinite Prandtl number and that newer theories [10,11] have to be taken into account when high Rayleigh numbers are studied.

Further research is needed to investigate the time-dependent flow at Rayleigh numbers above 10^{10}. Studying horizontal convection at higher Rayleigh numbers could help to investigate the scaling laws in more detail. In particular, a better determination of the scaling laws in the unsteady flow regime requires more runs at larger values of the Rayleigh number. Also, in realistic systems at infinite Prandtl number (e.g., glasses and geomaterials) the viscosity of the fluid strongly depends on the temperature. Therefore, a temperature-dependent viscosity is important for the simulation of very viscous horizontal convection. In test runs we employed a viscosity contrast of 10^4 between the cold and hot material. The asymmetric character is then even stronger and the flow structure is of course dependent on whether the forcing is applied to the bottom or top boundary.

To sum it up, we provided observation of time-dependent flow for horizontal convection at an infinite Prandtl number. Variations in the temperature forcing affect the strength of the circulation and heat flow as well as the Rayleigh number of the transition to time dependence. The step profile results in the strongest circulation and heat flow and is the first that transitions into the unsteady regime, while the linear profile represents a weaker forcing and therefore makes the convection more stable. The heat flux and circulation strength scaling laws are found to be similar to that of horizontal convection at finite Prandtl number and agree well with established theories.

ACKNOWLEDGMENTS

We thank two anonymous referees for their helpful comments as well as Thomas Wiesehöfer for valuable technical support.

[1] M. E. Stern, *Ocean Circulation Physics* (Academic, New York, 1975).
[2] G. O. Hughes and R. W. Griffiths, Horizontal convection, Annu. Rev. Fluid Mech. **40**, 185 (2008).
[3] P.-Y. Passaggia, A. Scotti, and B. White, Transition and turbulence in horizontal convection: Linear stability analysis, J. Fluid Mech. **821**, 31 (2017).
[4] H. Stommel, On the smallness of sinking regions in the ocean, Proc. Natl. Acad. Sci. USA **48**, 766 (1962).
[5] H. T. Rossby, On thermal convection driven by non-uniform heating from below: An experimental study, Deep Sea Research and Oceanographic Abstracts **12**, 9 (1965).
[6] H. T. Rossby, Numerical experiments with a fluid heated non-uniformly from below, Tellus A **50**, 242 (1998).
[7] H. Jeffreys, On fluid motions produced by differences of temperature and humidity, Q. J. R. Meteorol. Soc. **51**, 347 (1925).

[8] J. C. Mullarney, R. W. Griffiths, and G. O. Hughes, Convection driven by differential heating at a horizontal boundary, J. Fluid Mech. **516**, 181 (2004).
[9] W. Wang and R. X. Huang, An experimental study on thermal circulation driven by horizontal differential heating, J. Fluid Mech. **540**, 49 (2005).
[10] G. O. Hughes, R. W. Griffiths, J. C. Mullarney, and W. H. Peterson, A theoretical model for horizontal convection at high Rayleigh number, J. Fluid Mech. **581**, 251 (2007).
[11] O. Shishkina, S. Grossmann, and D. Lohse, Heat and momentum transport scalings in horizontal convection, Geophys. Res. Lett. **43**, 1219 (2016).
[12] O. Shishkina and S. Wagner, Prandtl-Number Dependence of Heat Transport in Laminar Horizontal Convection, Phys. Rev. Lett. **116**, 024302 (2016).
[13] S. Chiu-Webster, E. J. Hinch, and J. R. Lister, Very viscous horizontal convection, J. Fluid Mech. **611**, 395 (2008).
[14] F. Paparella and W. R. Young, Horizontal convection is non-turbulent, J. Fluid Mech. **466**, 205 (2002).
[15] A. Scotti and B. White, Is horizontal convection really non-turbulent? Geophys. Res. Lett. **38**, L21609 (2011).
[16] K. D. Stewart, G. O. Hughes, and R. W. Griffiths, When do marginal seas and topographic sills modify the ocean density structure? J. Geophys. Res. **116**, C08021 (2011).
[17] B. Gayen, R. W. Griffiths, G. O. Hughes, and J. A. Saenz, Energetics of horizontal convection, J. Fluid Mech. **716**, R10 (2013).
[18] R. W. Griffiths, G. O. Hughes, and B. Gayen, Horizontal convection dynamics: Insights from transient adjustment, J. Fluid Mech. **726**, 559 (2013).
[19] T. Tsai, W. K. Hussam, A. Fouras, and G. J. Sheard, The origin of instability in enclosed horizontally driven convection, Int. J. Heat Mass Transfer **94**, 509 (2016).
[20] B. Gayen, R. W. Griffiths, and G. O. Hughes, Stability transitions and turbulence in horizontal convection, J. Fluid Mech. **751**, 698 (2014).
[21] S. Grossmann and D. Lohse, Scaling in thermal convection: A unifying theory, J. Fluid Mech. **407**, 27 (2000).
[22] J. H. Siggers, R. R. Kerswell, and N. J. Balmforth, Bounds on horizontal convection, J. Fluid Mech. **517**, 55 (2004).
[23] G. J. Sheard and M. P. King, Horizontal convection: Effect of aspect ratio on Rayleigh number scaling and stability, Appl. Math. Model. **35**, 1647 (2011).
[24] R. X. Huang, Mixing and energetics of the oceanic thermohaline circulation, J. Phys. Oceanogr. **29**, 727 (1999).
[25] J. T. Houghton, *The Physics of Atmospheres* (Cambridge University Press, Cambridge, 2002).
[26] H. J. J. Gramberg, P. D. Howell, and J. R. Ockendon, Convection by a horizontal thermal gradient, J. Fluid Mech. **586**, 41 (2007).
[27] D. Zhao, Global tomographic images of mantle plumes and subducting slabs: Insight into deep earth dynamics, Phys. Earth Planet. Inter. **146**, 3 (2004).
[28] M. A. Coman, R. W. Griffiths, and G. O. Hughes, The sensitivity of convection from a horizontal boundary to the distribution of heating, J. Fluid Mech. **647**, 71 (2010).
[29] U. Hansen and A. Ebel, Experiments with a numerical model related to mantle convection: Boundary layer behaviour of small-and large scale flows, Phys. Earth Planet. Inter. **36**, 374 (1984).
[30] U. Hansen and A. Ebel, Time-dependent thermal convection—A possible explanation for a multiscale flow in the earth's mantle, Geophys. J. Int. **94**, 181 (1988).
[31] B. Blankenbach *et al.*, A benchmark comparison for mantle convection codes, Geophys. J. Int. **98**, 23 (1989).